Geophys. J. Int. (2008) **174,** 949–965 doi: 10.1111/j.1365-246X.2008.03841.x

Core-log integration studies in hole-A of Taiwan Chelungpu-fault Drilling Project

Yun-Hao Wu,[1] En-Chao Yeh,[2] Jia-Jyun Dong,[3] Li-Wei Kuo,[2] Jui-Yu Hsu[3] and Jih-Hao Hung[1]

[1]*Institute of Geophysics, National Central University, Taiwan. E-mail: jhhung@ncu.edu.tw*
[2]*Department of Geosciences, National Taiwan University, Taiwan*
[3]*Institute of Applied Geology, National Central University, Taiwan*

Accepted 2008 May 2. Received 2008 April 30; in original form 2007 January 23

SUMMARY

Taiwan Chelungpu-fault Drilling Project (TCDP) was initiated to understand the physical mechanisms involved in the large displacements of the 1999 Taiwan Chi-Chi earthquake. Continuous measurements of cores (including laboratory work) and a suite of geophysical downhole logs, including *P*- and *S*-wave sonic velocity, gamma ray, electrical resistivity, density, temperature, electrical borehole images and dipole-shear sonic imager, were acquired in Hole-A over the depth of 500–2003 m. Integrated studies of cores and logs facilitate qualitative and quantitative comparison of subsurface structures and physical properties of rocks. A total of 10 subunits were divided on the basis of geophysical characteristics. Generally, formation velocity and temperature increase with depth as a result of the overburden and thermal gradient, respectively. Gamma ray, resistivity, formation density, shear velocity anisotropy and density-derived porosity are primarily dependent on the lithology. Zones with changes of percentage of shear wave anisotropy and the fast shear polarization azimuth deduced from Dipole Shear-Imager (DSI) are associated with the appearance of fractures, steep bedding and shear zones. The fast shear wave azimuth is in good agreement with overall dip of the bedding (approximately 30° towards SE) and maximum horizontal compressional direction, particularly in the Kueichulin Formation showing strong shear wave velocity anisotropy. Bedding-parallel fractures are prevalent within cores, whereas minor sets of high-angle, NNW–SSE trending with N- and S-dipping fractures are sporadically distributed. The fault zone at depth 1111 m (FZA1111) is the Chi-Chi earthquake slip zone and could be a fluid conduit after the earthquake. The drastic change in fast shear wave polarization direction across the underlying, non-active Sanyi thrust at depth 1710 m reflects changes in stratigraphy, physical properties and structural geometry.

Key words: Earthquake source observations; Seismicity and tectonics.

1 INTRODUCTION

Understanding physical mechanisms in seismogenic zones that can nucleate large earthquakes has been a major subject in fault zone dynamics, and a number of scientific fault-zone drilling projects were thus initiated, such as the Corinth Rift Laboratory (CRL) in Greece (e.g. Cornet 2007), Drilling Active Faults in South African Mines (e.g. Reches & Ito 2007), Nojima fault scientific drilling program (after the 1995 Kobe earthquake), the San Andreas Fault Observatory at Depth (SAFOD) at Parkfield, CA, and the Nankai Trough drilling. Results of above drilling projects (e.g. Berchkhemer *et al.* 1997; Boness & Zoback 2004; Ito & Kiguchi 2005) improve our knowledge of active fault zones in various aspects, such as fault zone properties, deformation mechanisms, stress states, mechanical and chemical roles of fluids and physical properties of the crust. Studies of downhole logs, cuttings and cores provide crucial information of subsurface geology and direct evidence of physical properties and deformation mechanisms of the fault zones at depth.

The 1999 Taiwan Chi-Chi earthquake (M_w 7.6) is one of the world's most devastating earthquakes and caused severe property damage and more than 2000 casualties (see Kao & Chen 2000; Ma *et al*. 2000). The surface rupture extends over 90-km and along the north–south trending, west-vergent Chelungpu fault, which is a low angle (∼30°) thrust in the Western Foothills (e.g. Wang *et al.* 2000, 2002; Yu *et al.* 2005). Surface displacements are as large as 8–12 m (e.g. MOEACGS 2000; Yu *et al.* 2001; Lee *et al.* 2002) in the northern segment between Fengyuan and Dakeng area (e.g. Yang *et al.* 2000; Lee *et al.* 2001). To explore the mechanisms and physical properties involved in large displacements of the rupture fault, two holes (Hole-A of 2003 m and Hole-B of 1350 m in

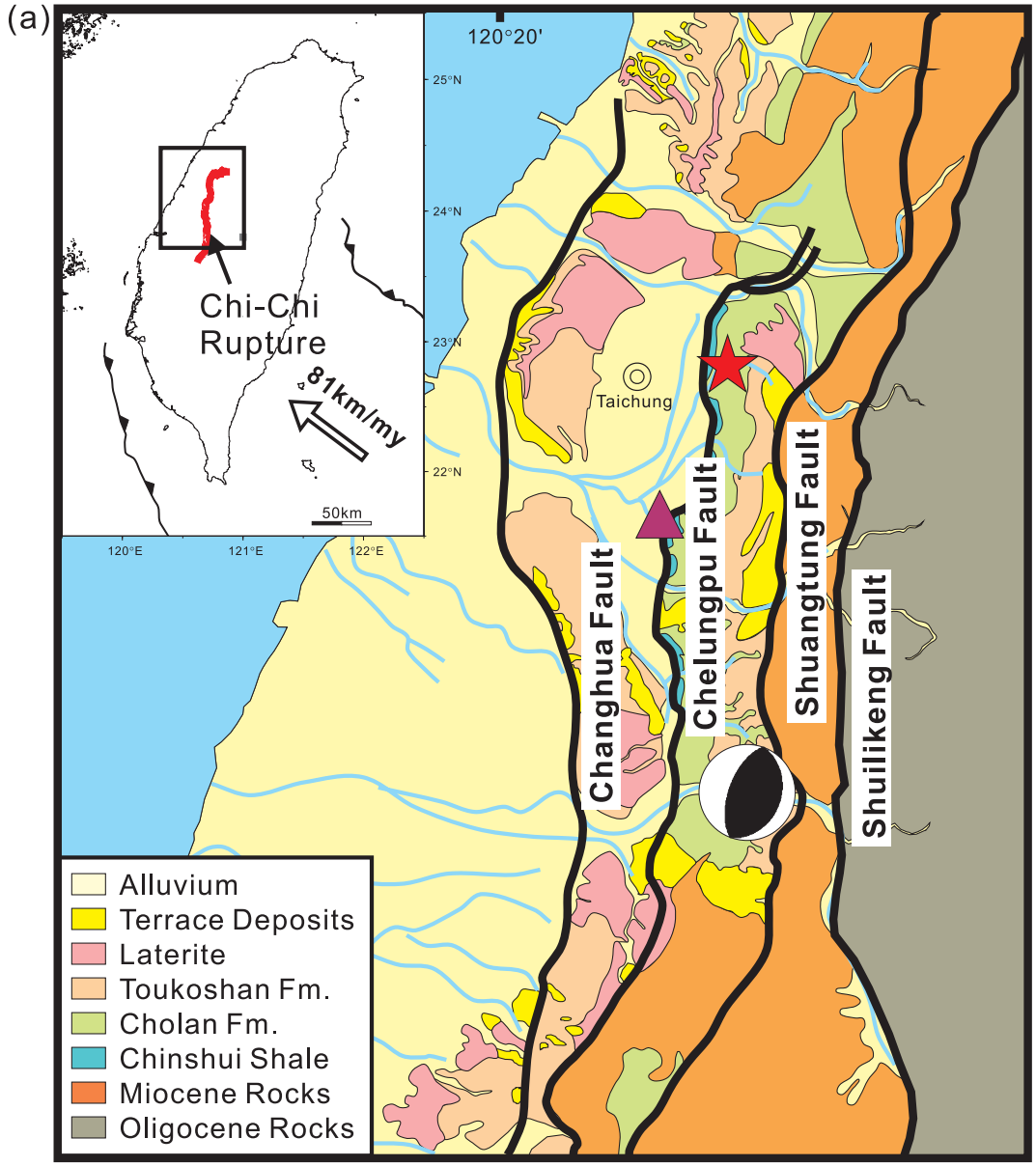

Figure 1. (a) Generalized geological map of western Taiwan. Star: location of TCDP drill site; triangle: Wufeng town; focal sphere: Chi-Chi earthquake epicentre. (b) Interpreted E–W trending structural cross-section across the drill site.

depth) of 40 m apart were drilled during 2004–2005 for Taiwan Chelungpu-fault Drilling Project (TCDP) at Dakeng, westcentral Taiwan, where large surface slip (∼10 m) was observed. Continuous coring and downhole wireline logging were completed from a depth of 500–2003 m (Hole-A) and 950–1350 m (Hole-B). Along with conventional logs, Dipole Shear-Imager (DSI) with *P*- and *S*-wave velocity and Formation MicroImager (FMI) and its predecessor, Formation MicroScanner (FMS) were also completed in Hole-A.

Previous studies using above data are extensive and include various aspects of mechanical, physical and chemical properties, such as *in situ* stress and strain, thermal structure, friction coefficient, porosity and permeability, fracture energy of the slip zone and fluid composition (e.g. Chen *et al.* 2005; Dong *et al.* 2005; Kitamura *et al.* 2005; Lockner *et al.* 2005; Louis *et al.* 2005; Lu & Chen 2005; Sone *et al.* 2005, 2007; Wang *et al.* 2005; Wu *et al.* 2005; Yabe *et al.* 2005; Lin *et al.* 2006; Ma *et al.* 2006; Hirono *et al.* 2007a, b). TCDP provides a unique opportunity for studies of core and logs and characterization of formation physical properties that are fundamental to above investigation but not yet detailed studied before. In this paper we synthesize results from cores, geophysical logs, high-resolution microresistivity images of the borehole wall and laboratory experiments of cores to characterize subsurface structure, fault zones, and physical properties of formations in Hole-A.

2 TECTONIC SETTING OF THE CHELUNGPU FAULT

The Taiwan mountain belt is a suture of the oblique convergent boundary between the Eurasian and Philippine Sea Plates (e.g. Barrier & Angelier 1986; Teng 1990; Lallemand *et al.* 2001; Malavieille *et al.* 2002). The South China Sea of the Eurasian Plate

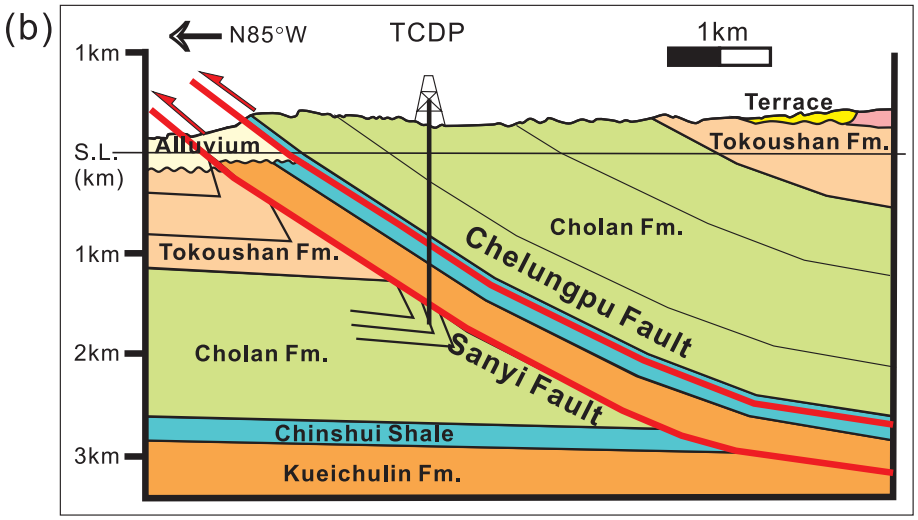

Figure 1. (*Continued*.)

subducts eastward beneath the Philippine Sea Plate in the south, producing the Luzon volcanic arc. The latter seated on the Philippine Sea Plate moves towards 306° with a velocity of 81 mm yr^{-1} (e.g. Yu *et al.* 1997) and collides with the Eurasian continental margin, raising the Taiwan island. The Philippine Sea Plate subducts beneath the Eurasian continental margin in the northeast of Taiwan, creating the Ryukyu Trench and Okinawa Trough. This progressive oblique collision and interaction between two subduction systems result in the active faulting within Taiwan mountain belt with numerous earthquakes and significant crustal deformation. Stratigraphic sequences cropping out in the westcentral Taiwan, from top to bottom, (Fig. 1a) include: Pleistocene Toukashan Formation (1–2 km thick; conglomerate and alternations of fluvial to shallow marine sandstone and siltstone), early Pleistocene–Pliocene Cholan Formation (1.5–2.5 km thick; monotonous alternating sandstone and siltstone), early Pliocene Chinshui Shale (∼300 m thick; shale and siltstone) and late Miocene-early Pliocene Kueichulin Formation (0.8–2 km thick; shallow marine sandstone and shale) (e.g. Ho 1988). Four major north–south trending, west-vergent, subparallel thrust faults from west to east are the Changhua, Chelungpu, Shuangtong and Shuilikeng faults, which form the imbricate structure in the Fold-and-Thrust Belt of western Taiwan (e.g. Suppe 1981; Davis *et al.* 1983).

The Chelungpu thrust runs parallel to the hanging-wall composed of the Chinshui Shale except near the northern segment, indicating that the fault plane is detached in the Chinshui Shale (e.g. Yue at al. 2005; Hung et al. 2007). In map-view (e.g. CPC 1982) south of Wufeng village, the Chelungpu fault emplaced the Chinshui Shale on top of the Tokoushan Formation and Holocene deposits. Towards north, the Chelungpu fault lies within the Chinshui Shale and is nearly parallel to the bedding (Fig. 1b). The Chelungpu fault is also a topographical boundary which separates the Taichung basin to the west from elevated foothills and mountains (e.g. Chang 1971), and was recognized as an active fault because of distinct geomorphic features (e.g. Bonilla 1977). Three other major faults (i.e. Changhua fault in the west, Shuangtong and Shuilikeng in the east) were not active during the Chi-Chi earthquake (e.g. Yu *et al.* 2001; Hung *et al.* 2002; Pathier *et al.* 2003), thereby out-of-sequence thrusting occurs in this imbricate system (e.g. Kao & Chen 2000).

3 DATA ACQUISITION AND METHODOLOGY FOR CORE-LOG INTEGRATION

Cores with diameter of 3.26 inches (8 cm) were retrieved from Hole-A with a bit size of 6.22 inches (∼16 cm). Casing shoes were located at depths of 661 and 1300 m, respectively (Appendix A). Cores were marked with reference lines and scanned with digital camera in slab mode and unrolled mode after wrapped in heat-shrinkage plastic tubes. Core images were then aligned with the reference lines (parallel to the downdip direction of bedding, or azimuth 105° on average) and stacked in stratigraphic column for structural analyses of bedding and fractures (Fig. 2). Continuous physical properties of cores were also measured in the laboratory for detailed correlation between cores and logs.

Downhole wireline logs (Appendix B) were obtained from two industrial companies—Schlumberger (SLB) and Chinese Petroleum Corporation (CPC), and one scientific team—International Continental Scientific Drilling Program (ICDP). The hole-deviations are less than 4° above a depth of 1600 m but gradually increase downward to 12° at depth of 1865 m, below which the logging tools were not able to reach the hole-bottom because of unstable borehole wall. Surveyed logging tools include 4-arm caliper (CAL), Dual Phase Induction Log (DPIL), SpectraLog (SL), Temperature/Tension/Mud Resistivity (TTRM) and Digital Acoustic (DAC) (trademarks of Baker Atlas; operated by CPC); Array Induction Tool (AIT), Three-Detector Lithology Density (TLD), DSI, FMS and FMI (trademarks of Schlumberger); Mud temperature-total gamma ray-resistivity (MP), Natural Gamma Radioactivity (GR), Acoustic Imaging of the borehole wall (FAC40) and Induction of Resistivity-sonic Velocity (TS-BSDLL, TS-DLL) (trademarks of ICDP). All logs were sampled at a rate of every 15 cm interval. Formation resistivity was measured by both AIT and DPIL over the same interval, therefore, DPIL results are shown here unless AIT is specified. In general, both tools show coherent results at common depth section.

Logging data is reported by wireline depths, whereas drilling depths are used in core data. The FMI images serve as a link to correlate features in cores and log databases. By correlating the total natural gamma-ray curves surveyed in each run among conventional and FMI/FMS logs, a depth shift is imposed among conventional

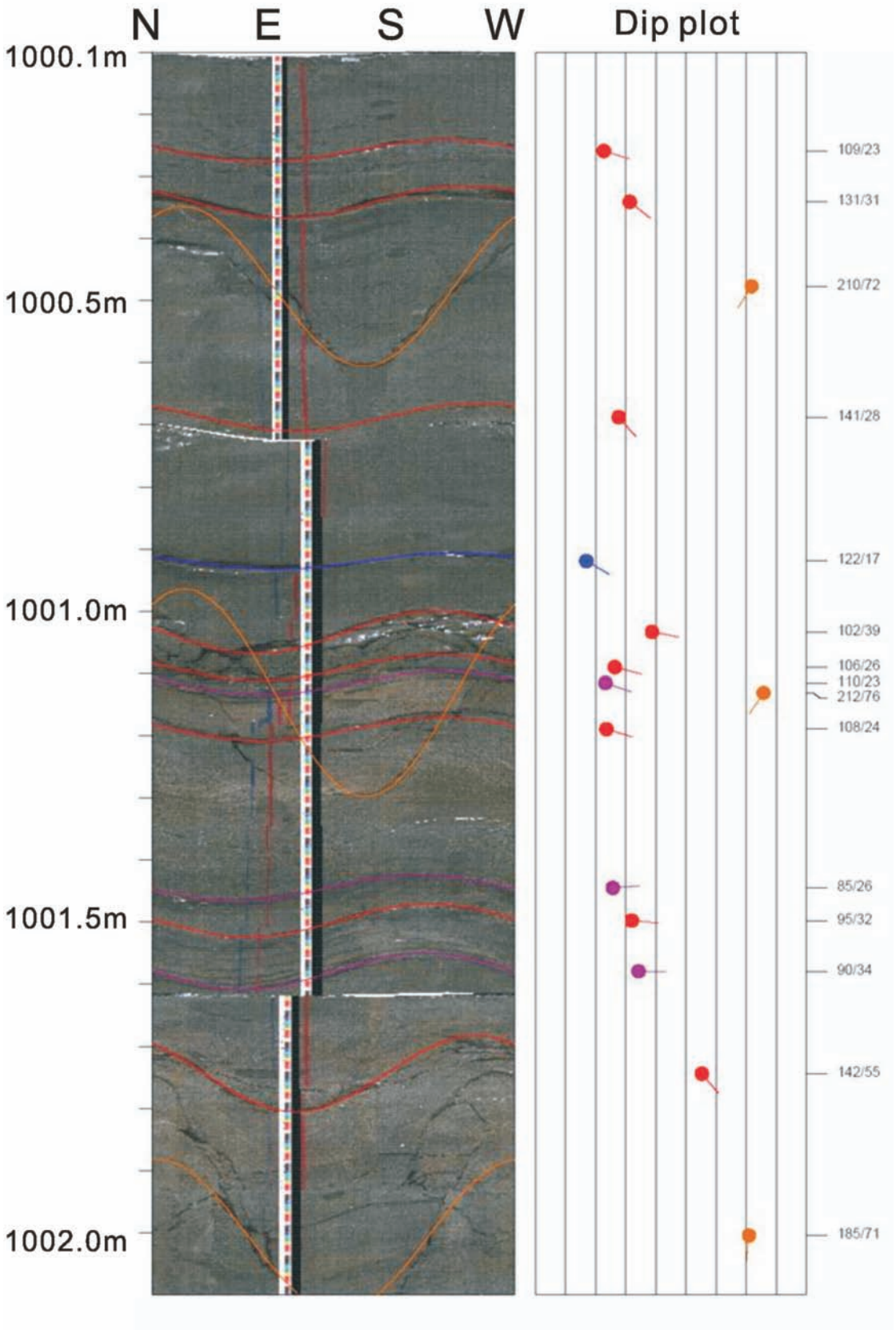

Figure 2. Unrolled core image and interpreted structures at depth interval of 1000.1–1002.0 m. Fractures and beds appear as sinusoids on the left and their corresponding tadpoles on the right. Various structures are in different colours.

logs. The unrolled core images were then laid-out side-by-side with conventional logs and the borehole FMS/FMI images to produce a visual correlation between core and log data, and thus depth match among logs, unrolled core-images and cores can be made. The joint core and log integration is utilized to: (1) calibrate core and log data; (2) extract particularly subsurface physical information such as lithological boundaries and (3) predict the lithology at places where core recovery is incomplete (e.g. Lofts & Bristow 1998; Major *et al.* 1998). Results of core-log integration are discussed in the section of physical properties and log units.

Two important physical properties, porosity and Bulk Volume of Water (BVW), can be deduced from log data. Porosity (ϕ) can be derived from density model (Schlumberger 1989):

$$\phi = \frac{(\rho_{ma} - \rho_b)}{(\rho_{ma} - \rho_{fl})}, \quad (1)$$

where ρ_{ma},ρ_b, ρ_{fl} are matrix density, bulk density and formation fluid density, respectively. The BVW can be computed by BVW $= \phi \times S_w$, and S_w can be, in turn, determined from Archie's equation:

$$S_w^n = \frac{a}{\phi^m}\frac{R_w}{R_t}, \quad (2)$$

where S_w is water saturation; R_w is formation water resistivity; R_t is true formation resistivity; a is constant; m is cementation factor and n is saturation exponent.

The parameters of a, m and n can be determined empirically, and values of 1, 2 and 2, respectively, were used in this study for compacted formations. R_t is recorded in log data. Measured resistivity of drilling mud is 4 ohm-m at 25 °C. Assuming $S_w = 1$ in water zones, then R_w can be estimated from ϕ and R_t and equals to an average value of 0.1 ohm-m.

4 SUBSURFACE STRUCTURE, PHYSICAL PROPERTIES AND LOG UNITS

The regional dip of bedding above 1710 m, identified from both cores and FMI (or FMS) logs, is about 30 degrees towards the SE. Nevertheless, local azimuthal variations and dip changes appear across fault zones. A drastic increase of structural dip from 20–40° to 60–80° occurs below FZA1856, where steep to overturned beds extend to the hole bottom (see Hung *et al.* 2007). A total of 11 fault zones were identified with locations shown by dash lines (Fig. 3 and Appendix E). The top 4 fault zones (red arrows) within the Chinshui Shale are associated with the Chelungpu fault system, and the rest fault zones (blue arrows) are related to the Sanyi fault system. Among them, the fault zone at 1111 m depth (FZA1111) is interpreted to be the rupture fault during the Chi-Chi earthquake on the basis of distinct deformed textures (fault gouges) in the core (e.g. Ma *et al.* 2006). The core observation is also substantiated by physical properties from logging, which is discussed in the log unit section. Fracture distribution is closely related to the fault zone development. Observed fractures in the core can be divided into four orientations based on the dip azimuth: 45–135 (East, marked 'E'), 135–225 (South, marked 'S'), 225–315 (West, marked 'W') and 315–45 (North). Five categories of faults (dip azimuth/dip) can be grouped in above orientations: (1) thrust (E, 105/30), (2) left-lateral (N, 015/30–80), (3) right-lateral (S, 195/30–80), (4) normal (105/5–10) and (5) backthrust (W, 285/40–50) (see Yeh *et al.* 2007). Bedding-parallel fractures are dominant in the core, whereas NW-trending fracture sets are sporadically distributed (Fig. 3 column-L). Locally, steep (40–80°) north-dipping fractures appear at the interval of 1010–1350 m (Fig. 3a, 4th–6th in column-L) or the Chinshui Shale (1013–1300 m) (e.g. Hung *et al.* 2007; Lin A. *et al.* 2007); whereas low-angle (30–40°) south-dipping fractures occurred above FZA1111 (Fig. 3a, 4th–5th in column-L). The overall fracture density increases approaching FZA1111.

The FMS/FMI calipers provide borehole geometry and condition. Borehole washouts (e.g. Plumb & Hickman 1985), are common from 500 to 1000 m (Fig. 3a, column-A). Other types of borehole failure, such as key seat and borehole breakouts, appear from 1300 m to the log bottom. Transient mud temperature measured immediately after drilling from 500 to 1842 m display a relatively low gradient of 10 °C km^{-1}. Although no thermal anomaly was observed, Kano *et al.* (2006) reported a slight heat signal around the FZA1111 during repeated temperature measurements 6 months after the completion of drilling.

In this study, the clean sand and shale baselines are defined through correlation between qualitative core observation and quantitative gamma ray radiation which is proportional to the clay content (Fig. 4). Values of 75 API and 105 API are adopted as clean sandstone and shale baselines, respectively, and in between is the siltstone. Gamma-ray curves in sandstones of the Cholan Formation show a half-convex funnel pattern (e.g. Doveton 1994) and corresponding to an upward increase in both grain size and sandstone to shale ratio (Fig. 3 column-E) (e.g. Hung *et al.* 2007). S_w is generally low in sandstone but high in shale, probably because of higher bounding water content in the shale (Fig. 3 column-H). Similarly, the computed BVW is consistently high (∼0.2) in the Chinshui Shale and Kueichulin Formation but various low values in the Cholan Formation (Fig. 3 column-C).

Higher resistivity and lower density are generally observed in sandstone than in shale (Figs 3a and b). Thereby, the overall formation resistivity is higher in the Cholan and Kueichulin Formation than in the Chinshui Shale. This can be further evidenced by cross-plots of resistivity versus gamma ray (Fig. 5), where a negative slope of gamma-ray radiation with respect to resistivity is observed. Besides conventional resistivity logs, FMS/FMI provide detailed resistivity data, and therefore, correlation among the FMS/FMI images, resistivity, natural gamma ray and core lithology can be made (Fig. 3 columns-E&**K**). As expected, the mean resistivity is relatively lower in the Chinshui shale than in the Kueichulin Formation (Fig. 3 column-B).

In a broad view, three are significant low resistivity zones surveyed by the magnetotelluric method (see Chiang *et al.* 2008). Two shallow zones are associated with subsurface aquifers (see Yeh *et al.* 2007). The deep one corresponds to the depth interval of the Chinshui Shale, and the lowest resistivity (less than 10 ohm-m) appear at FZA1111 (Fig. 6). A drastic increase in resistivity across FZA1581 corresponds to the change of the stratigraphy from the Kueichulin Formation to the Cholan Formation (e.g. Yeh *et al.* 2007).

The DSI tool measures formation velocity, including V_p and V_s, and the results show that both V_p and V_s increase slightly with depth (Fig. 3 column-G). Other mechanical properties can be deduced from DSI logs include Poisson's ratio (PR, or υ), defined by $\upsilon = 0.5(\sigma^2 - 2)/(\sigma^2 - 1)$, where $\sigma = V_s/V_p$ (Fig. 3 column-F) and percentage of shear wave velocity anisotropy, defined by $\gamma = (Vs^2_{fast} - Vs^2_{slow})/Vs^2_{slow}$ (e.g. Thomsen 1986) as an indicator of degree of fracturing. The γ values increase with the content of sandstone and can be as high as 30–40 per cent (Fig. 3 columns-D&E). Relatively uniform azimuth of the Fast Shear Horizontal (FSH) direction in the Kueichulin Formation (Fig. 3 columns-J&**L**) indicates that significant shear wave anisotropy is partially affected by

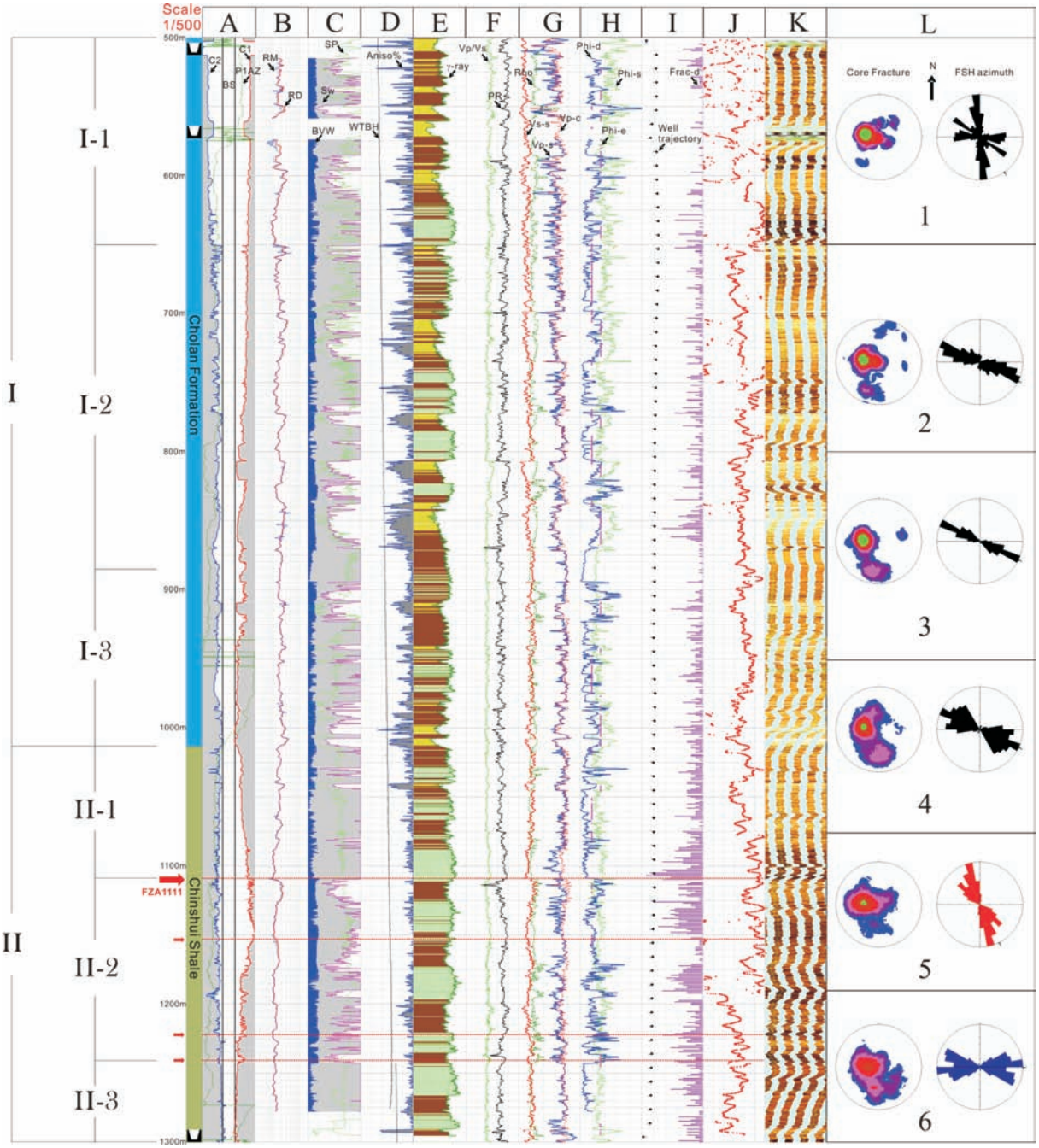

Figure 3. Composite figure of downhole logs. Columns from left- to right-hand side: log units, sedimentary sequences; A: hole geometry and P1 azimuth; B: resistivity (CPC); C: S_w and BVW, D: temperature and percentage of shear wave velocity anisotropy, E: gamma-ray derived lithology; F: PR (υ) and V_p/V_s, G: DT and density, H: porosity, I: well trajectory and fracture frequency; J: FSH azimuth; K: borehole-wall microresistivity images from resistive (light colour) to conductive (dark colour); L: Contour plots of lower-hemisphere stereographic projection of poles to fractures and rose diagram of FSH azimuth. A total of 9 zones are divided based on the distribution of fast shear polarization azimuth. Colours indicate percentages of concentration from the lowest (blue) to the highest (lime, 32 per cent) with contour intervals of 1, 2, 4, 8 and 16 per cent (see also Appendix C–F).

the lithology or the degree of fracturing. Other factors such as fault zones and anisotropy of the stress field could also locally change the degree of anisotropy and fast shear polarization direction.

The geophysical logs can be further classified into four major units (with minor sections) on the basis of trend, character and discontinuity (Appendix D). Details of each unit are described in below.

4.1 Unit I (Cholan Formation)

The gamma-ray histogram indicates that sandstone, siltstone and a small amount of shale appear in the Cholan formation (Fig. 4b). The mean value of gamma ray is 85 API with a standard deviation of 17. Caliper log shows that at shallow depths the borehole is much larger than the bit size but became stable and in gauge as

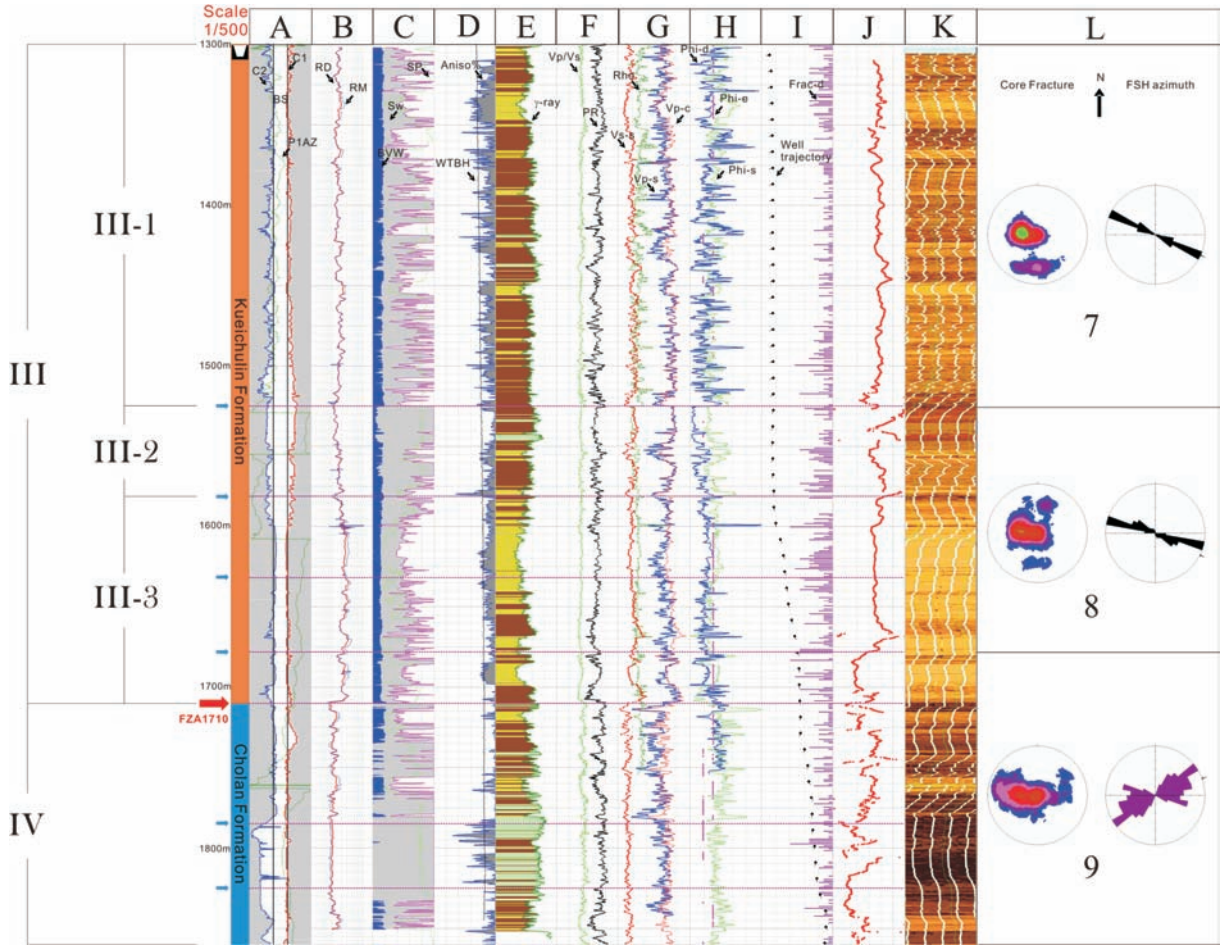

Figure 3. (*Continued*.)

depth increases. Two aquifers at depths of 140–150 and 390 m (see Yeh *et al.* 2007), poor cementation and fractured zones may cause bad hole conditions of washout and caving. Unit I can be further divided into three sections with boundaries at 660 and 870 m, which corresponds to the change of lithology, and porosity and PR, respectively. Sandstone in section I-2 is characterized by high resistivity (25–35 ohm-m) and PR (0.3–0.4). Density and PR range between 2.3–2.4 g cm^{-3} and 0.2–0.3, respectively, corresponding to more indurate sandstone in section I-3. Sandstone porosity measured in the laboratory is on average of 16 per cent and is comparable to the values obtained from the density model but less than those (∼20 per cent) derived from the sonic log using Wyllie model (Schlumberger 1989). The S_w is estimated to be 0.8–1 in muddy sandstone and 0.2–0.5 in clean sandstone, but the BVW is, in contrast, slightly higher in clean sandstone than muddy sandstone. The randomly oriented FSH azimuth in section I-1 indicates that the strongly bioturbated muddy sandstone is relatively isotropic. Two shear zones at depths of 780 and 870 m are recognized by fault gouge, moderate to highly fractured damage zone, and low core recovery. Concurrent physical properties in the fault zones include decrease in wave velocity and PR, increase in resistivity, and high variability in FSH azimuth.

4.2 Unit II (Chinshui Shale)

Shale and muddy sandstone are dominant in the Chinshui Shale (1013–1300 m, Fig. 4c) with Gamma-ray radiation of 105 ± 12 API. Severe washouts occurred in the relatively soft intervals.

4.2.1 Section II-1

Section II-1 is primarily composed of shale and siltstone and characterized by high gamma-ray radiation, density and S_w but low porosity and BVW. Fracture density around FZA1111 is the highest among fault zones in Hole-A. Anomalies of physical properties associated with FZA1111 include (Fig. 6): (1) low density, (2) low resistivity, (3) low BVW, (4) high porosity, (5) low sonic velocities but high PR and V_p/V_s and (6) low shear wave anisotropy. That the interval of low resistivity and sonic velocities but high PR and V_p/V_s corresponding to the length of fault gouge indicates that the fault gouge zone, mainly composed of clay minerals, is weak and contains large amount of formation fluid with low resistivity (e.g. Song & Kuo 2006; Hirono *et al.* 2007b).

4.2.2 Section II-2

Calcite-cemented siltstone appears in the core and extends for 15 m in the footwall of FZA1111. At the same interval, both core and gamma-ray radiation show that the rock type changes abruptly from clay gouge to host rock. The decrease in S_w and PR but increase in resistivity, porosity and BVW are common characters of intact host rock. From FZA1111 to FZA1241, extremely high

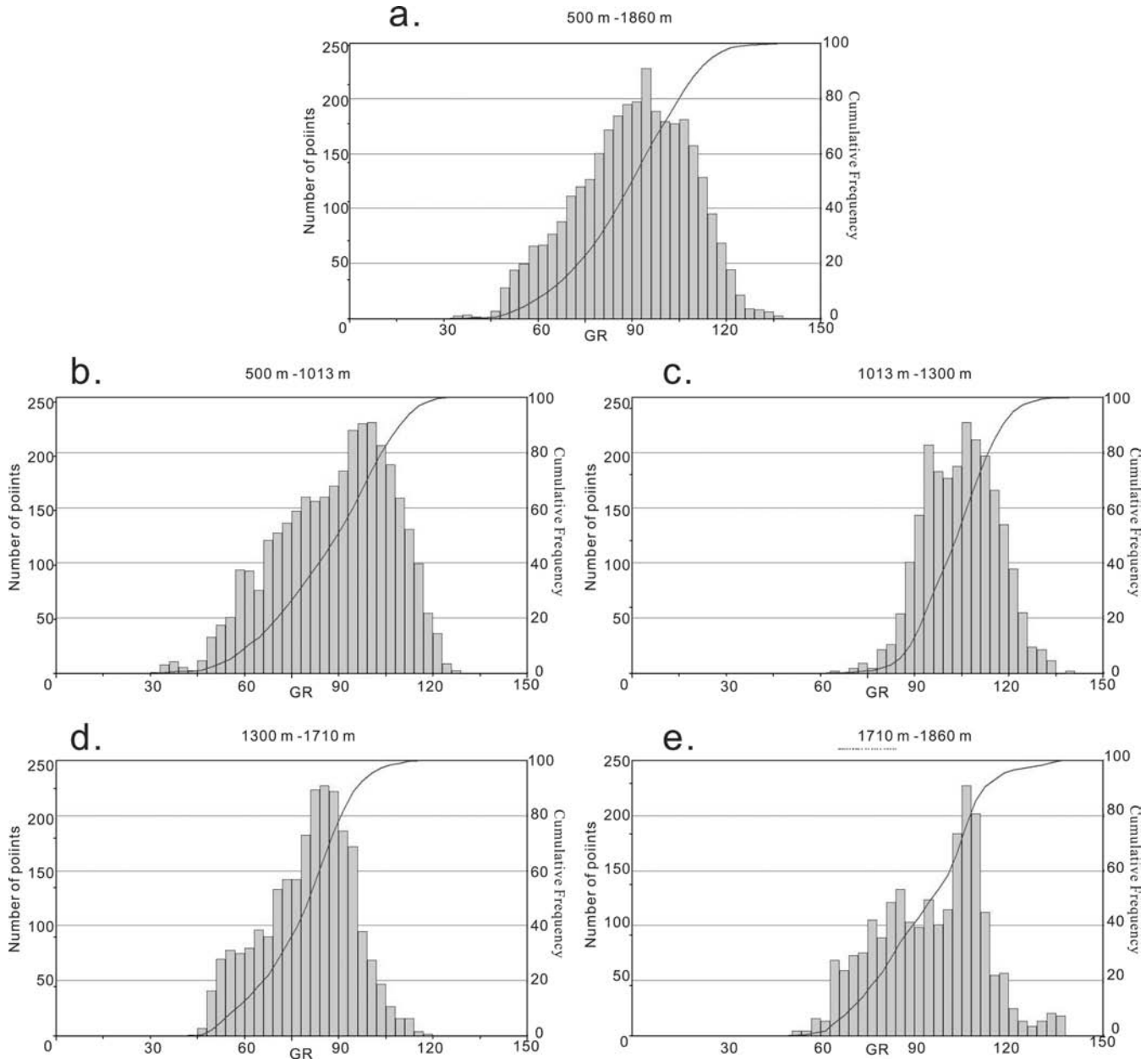

Figure 4. Histograms of gamma ray values and their associated cumulative curves showing proportions of clean sandstone and muddy/shaly sandstone at various depth intervals. (a) 500–1860 m; (b) 500–1013 m (Cholan Formation): high percentage of muddy or shaly sandstone; (c) 1013–1300 m (Chinshui Shale): high content of shale; (d) 1300–1710 m (Kueichulin Formation): clean sand with thin layer siltstone being the major component and (e) 1710–1860 m (repeated section of the Cholan Formation): alternating muddy sandstone as those in (b).

porosity in shale/siltstone might be attributable to secondary origin such as fracturing. Core observations and low core recovery at depths of 1190–1210 m indicate moderate to highly fracturing in this interval, and there probably exists another shear zone. An ancillary feature across this shear zone is that there is about 30° changes in FSH azimuth. From stereonets of fracture distribution, this change can be attributable to more high-angle, N-dipping strike faults below the shear zone (Fig. 3 column-L, zone 6) compared to NE-dipping dominant fractures in zone 5.

4.2.3 Section II-3

Physical properties of rock are relatively uniform from FZA1241 to 1300 m compared to sections of II-1 and II-2. Relatively high values in gamma-ray, S_w and density but low in BVW, porosity and PR suggest that siltstone at this interval is probably dry, dense and less deformed.

4.3 Unit III (Kueichulin Formation)

Unit III is primarily composed of thick beds of alternated sandstone and siltstone sequences. The increase in porosity and resistivity but decrease in S_w with depth implies less fluid content as degree of compaction increases. Two subunit boundaries (1525 and 1581 m) can be assigned by changes in resistivity, BVW, S_w, PR, density, V_p, porosity and FSH.

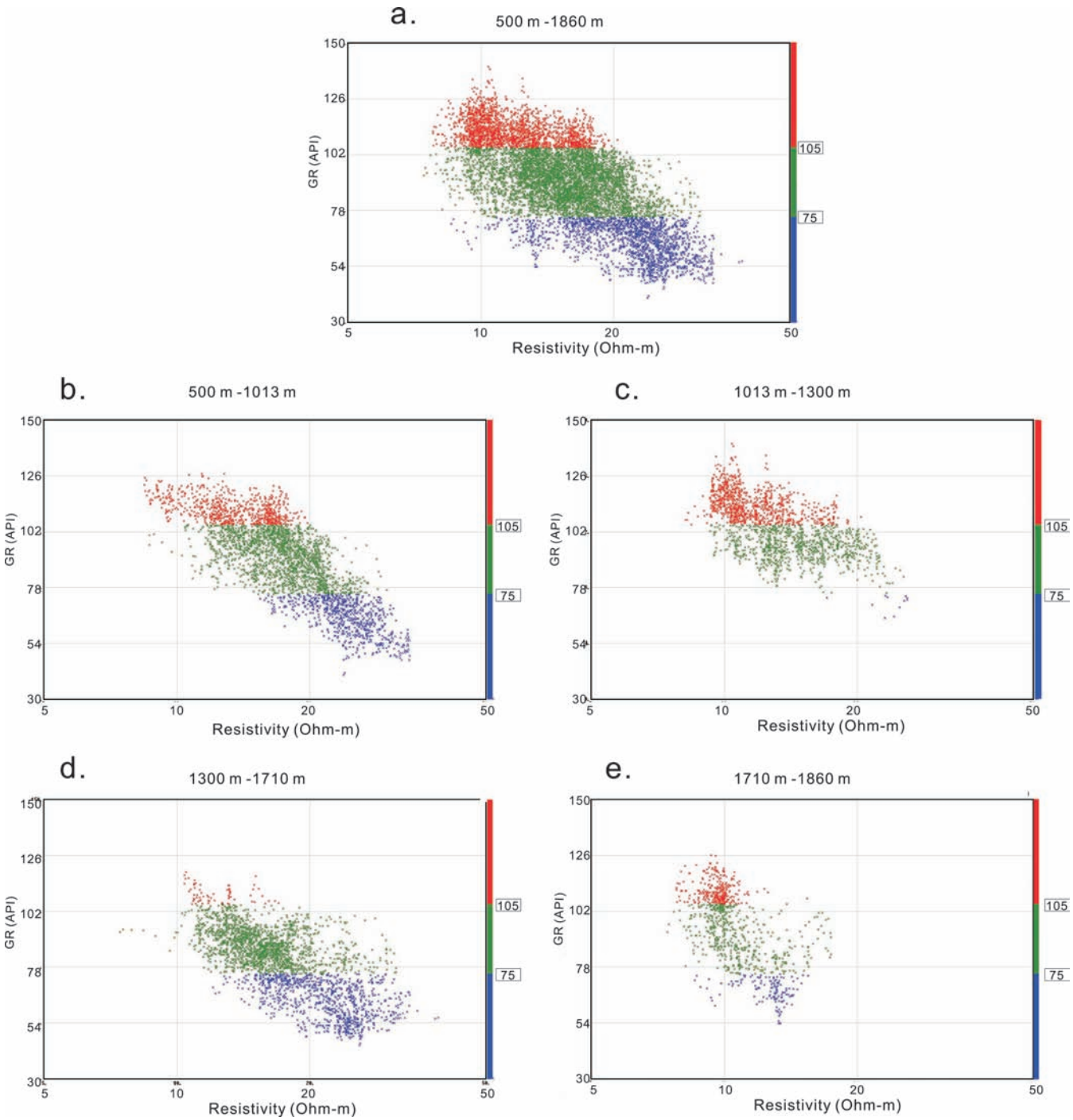

Figure 5. Cross plots of deep induction resistivity to gamma ray radiation: (a) 500–1860 m, (b) 500–1013 m (Cholan Formation), (c) 1013–1300 m (Chinshui Shale), (d) 1300–1710 m (Kueichulin Formation and (e) 1710–1860 m (Cholan Formation).

4.3.1 Section III-1

Alternated beds of clean and muddy sandstone with a gamma ray value of 80 ± 14 API are dominant from 1300 m to FZA1525 (Fig. 4d) and result in high variation of S_w. The mean BVW value is higher in this section than in unit II. Furthermore, high percentage of shear velocity anisotropy could be associated with the development of microcracks (e.g. Louis *et al.* 2005). Relatively low PR and uniform calipers suggest unit III-1 is well compacted and lack of shear/fault zones.

4.3.2 Section III-2

The FZA1525 is a boundary in both physical properties and rock type. Similar to FZA1241 in section II-3, abrupt changes in gamma-ray, resistivity, FSH azimuth, density and lithology occurred across FZA1525. Resistivity is relatively low in FZA1525, below which it increases in the footwall of host sandstone. Rock type in section III-2 is between siltstone-dominant section III-1 and sandstone-dominant section III-3 in terms of gamma-ray and resistivity.

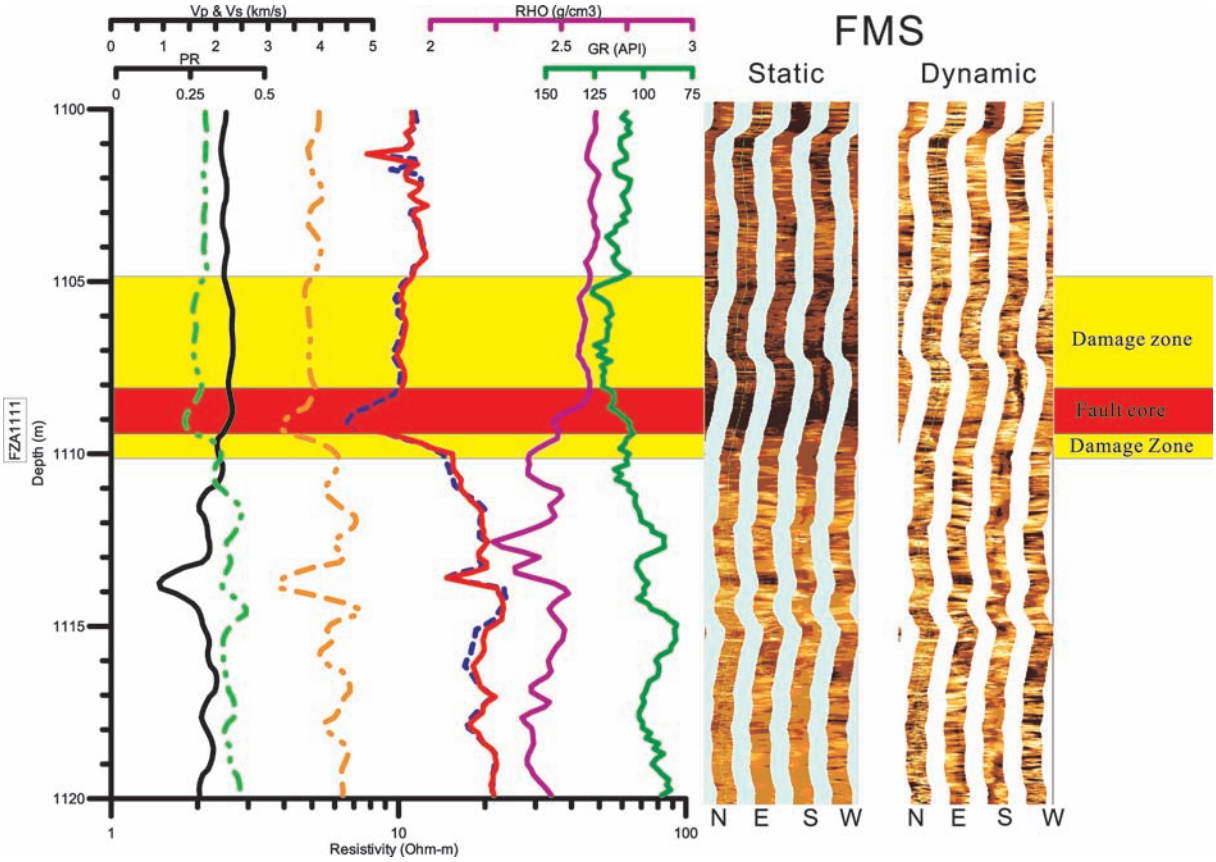

Figure 6. Rock physical properties near FZA1111. The fault zone (red zone) is composed of ∼1 m fault gouge and characterized by the lowest value of sonic velocity and resistivity in Hole-A. FMS images also show a gradational change from conductive in the clay-rich fault core, to less conductive in the damage zone and resistive in undeformed host rocks. The decrease in PR along with increase in resistivity delineates the boundary between the host intact rock and FZA1111. Black solid line: PR; green and orange break: V_p and V_s; solid red and blue: RD and RM, light purple: Rho; green solid: GR.

4.3.3 Section III-3

Relative to section III-2, resistivity and borehole deviation changes noticeably from FZA1581 downwards in section III-3. This section contains clean sandstone beds with the highest resistivity in Hole-A. The hole-trajectory starts to deviate from vertical, and the deviations increase with depth (see Fig. 3 column-I). Although the distribution of FSH azimuth is quite uniform, some old slip zones (FZA1632, FZA1679) appear locally in this section (e.g. Hung *et al.* 2007; Yeh *et al.* 2007).

4.4 Unit IV

FZA1710, also the Sanyi main thrust fault zone (e.g. Hung *et al.* 2007), is a significant discontinuity in stratigraphy, structure and physical properties. Cores below FZA1710 consist of loose, undercompacted, grey-colour siltstone to medium-coarse grained sandstone with mean gamma ray of 95 ± 17 API (Fig. 4e). Characteristics of these sandstones are similar in lithology to surface exposed Cholan Formation. Reworked Miocene fossils and nannofossil assemblages (Wu *et al.* 2007) also indicate that the footwall of the Sanyi fault is made up of repeated Cholan formation. Along with increasing regional bedding dip with depth, an abrupt change of physical properties occurred across FZA1710, below which values of resistivity, density and sonic velocities (V_p and V_s) are significantly reduced by 50, 3, 18 and 25 per cent, respectively. Relatively high BVW and low resistivity in both log data and laboratory measurements from cores indicate that unit IV contains large amount of fluid and also high permeability (see Hung *et al.* 2007). The predominant trending of FSH also changes from WNW–ESE to NE–SW across this boundary.

5 DISCUSSION

5.1 Porosity from various methods

Porosity is one of the fundamental physical properties of the rock and can be measured in the laboratory or derived from density or sonic logs. We apply the revised equations of Schlumberger (1989) to compute density porosity and Wyllie sonic porosity. The density porosity was estimated using clay and dry grain density measured in the laboratory (Kuo & Song 2005; Dong *et al.* 2007). Generally, sandstone porosities are comparable either measured in the laboratory or derived from density logs, but both are less than that derived from the sonic log using Wyllie model. The density-derived porosity in section II-2 is anomalously higher than other units and measurements in the laboratory (Dong *et al.* 2008). Fracture zones may cause this result.

5.2 FSH azimuth

There are several known causes of shear wave anisotropy in rocks (e.g. Johnson 1967; Crampin 1986; Christensen & Mooney 1995;

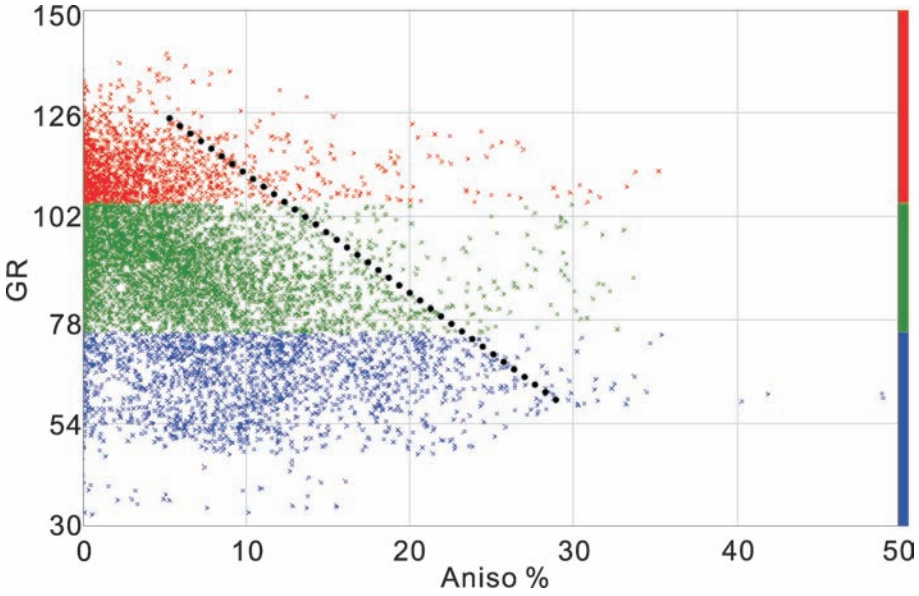

Figure 7. A cross plot of percentage of shear wave velocity anisotropy with respect to gamma ray radiation. Red, green and blue dots are shale (gamma ray API > 105), siltstone or muddy sandstone and clean sandstone (API < 75), respectively. The percentage of shear wave velocity anisotropy is inversely proportional to the API value, with a linear trend of Gamma ray = 141.7–2.9 Aniso% near the upper boundary.

Esmersoy *et al.* 1995; Bones & Zoback 2004, 2006; Crampin & Peacock 2005): (1) anisotropic *in situ* stresses which cause the preferred closure of microfractures and generate a fast direction parallel to the regional maximum horizontal stress (S_{Hmax}); (2) alignment of macrofractures without stress effects; (3) dilatancy of stress-aligned fluid-filled microcracks that produce the fast direction parallel to S_{Hmax}; (4) alignment of minerals or grains; (5) structural anisotropy due to layering (bedding planes) in sedimentary rocks (sedimentary fabrics) and (6) borehole shape or azimuth of borehole ellipcity acted by circumferential planar stress. The DSI has a low-frequency dipole source with frequency of 0.8–5 kHz frequency (e.g. Schlumberger 1995). As a result, the shear wave splitting would be highly sensitive to the anisotropic elements over tens of centimetre scale.

Analyses of the FSH azimuth from 500 to 1860 m show that the prevailing FSH azimuth is consistent with the dip direction of sedimentary structure or regional maximum compressional axis (e.g. Hung *et al.* 2007), particularly at zones where stereonets of facture distribution are less dispersed (column-L, zones 3, 7 and 8). Alignment of mineral grains or fluid-filled dilatational microcracks is unlikely since no preferred orientations of veins or minerals are observed either in the cores or thin sections. Because shear wave anisotropy displays a preferred orientation at high angle to regional trend of sedimentary beds and faults, the bedding-parallel fractures with dip less than 30–40° do not impose shear anisotropy for a vertical well. On the other hand, shear waves propagating through steep beds will split, and consequently, the NE–SW trend of fast shear polarization below 1710 m (column-L, zone 9) could be due to steep N to NE–SW trending and east-dipping beds. High-angle ENE-dipping fractures could contribute the change of FSH azimuth. For example, the FSH azimuth rotates clockwise about 30° in zone 5 compared to adjacent zones above and below, and it can be explained by either lacking of south-dipping fractures or combined effects mentioned above. Similarly, a concentrated group of nearly N-dipping fractures (or strike faults) are associated with a second set of nearly E–W trending FSH in zone 6. Therefore, the FSH azimuth can be associated with the trend of *in situ* stress-induced cracks (e.g. Lin W. *et al.* 2007).

Locations of abrupt change of FSH azimuth generally correspond to intervals of low core recovery as a result of fracturing. Therefore, the FSH azimuth is highly affected by facture density. A cross plot of gamma ray radiation with respect to percentage of shear velocity anisotropy indicates a tendency of negative linear relationship, Gamma ray = 141.7–2.9 Aniso%, near upper boundary (Fig. 7). This implies crack density is higher in the sandstone than in the muddy sandstone (see also Louis *et al.* 2005). This may explain that significant anisotropy and uniform FSH azimuth (N115°) are prevalent in the Kueichulin Formation which is composed of mainly coarser sandstone.

5.3 Fracture distribution

There are noticeable discrepancies in fracture distribution derived from between unrolled core images and borehole images in our studies as the FMS image covers only 55 per cent of the borehole wall with a hole-diameter of 16 cm (Fig. 8). Furthermore, thick, steep fractures can be better resolved in borehole images, whereas core images can show small, low-angle dipping fractures. Despite better coverage in core images, fracture density manually picked from unrolled images would not truly respond at the places of low core recovery or highly fractured. They are complementary to each other although neither technique is perfect. This inconsistency in fracture analysis from core and borehole images are also noted in other drilling project (e.g. Tezuka & Niitsuma 2000).

6 CONCLUSION

This study integrates data from downhole geophysical logs and cores to characterize physical properties of the formations in the Hole-A of TCDP scientific boreholes. We have documented subsurface structures and physical properties with depth, and the fault zone activated during the Chi-Chi earthquake. A total of 10 log units,

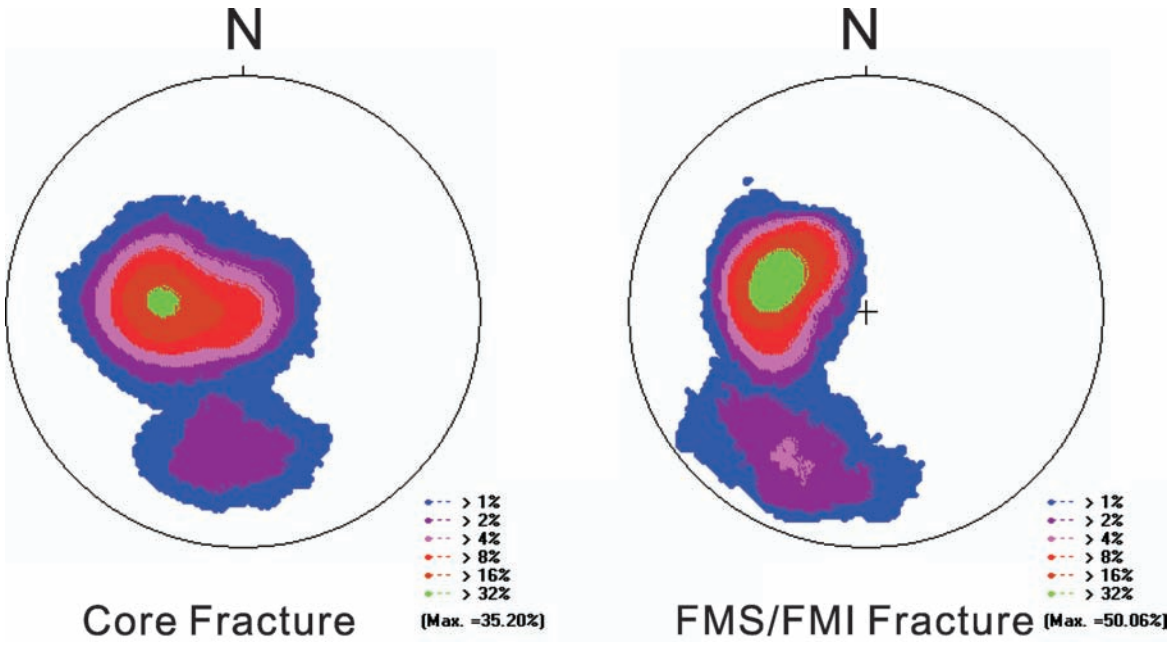

Figure 8. Stereoplots of poles to fractures picked from unrolled core images and borehole images in the intervals from 500 to 1860 m. There are minor discrepancies between deviation-corrected core images and FMS/FMI images.

each with consistent properties, are divided. *P*- and *S*-wave velocities and temperature are increasing with depth in general. Gamma ray, resistivity, density and shear wave anisotropy are primarily dependent on the lithology. Among all fault zones, FZA1111, characterized by thick clay gouge with anomalously low resistivity and density, and high Poisson's ratio and BVW, is the slip zone during the Chi-Chi earthquake. Perturbations in FSH azimuth in the interval of 1078–1190 m are associated with the presence of high-angle, NNW–SSE trending (ENE-dipping) fractures and lack of WNW–ESE trending (N–S dipping) fractures. Drastic changes in both shear wave anisotropy and azimuth of fast shear wave polarization across the Sanyi thrust fault at 1710 m are associated with changes in stratigraphy, physical properties and structural geometry.

ACKNOWLEDGMENTS

We thank participants and crew of the TCDP Project, particularly on-site assistants and students from NCU and NTU. We also thank two anonymous reviewers for clarifying this paper, B. Chao for English revision, G. Rafat for core image analysis, and T. Minawa, J. Lemains, C.M. Wang for log data consultation. Funding of TCDP is primarily from National Science Council (NSC), Taiwan, under the contract of NSC91-2119-M-008-030 and partially from the International Continental Scientific Drilling Program (ICDP). This study was financially supported by NSC (contract number NSC94-2119-M-008-009).

REFERENCES

Barrier, E. & Angelier, J., 1986. Active collision in eastern Taiwan: the Coastal Range, *Tectonophys.,* **125,** 39–72.

Berckhemer, H. *et al.*, 1997. Petrophysical properties of the 9-km-deep crustal section at KTB, *J. geophys. Res.,* **102,** 18 337–18 361.

Boness, N.L. & Zoback, M.D., 2004. Stress-induced seismic velocity anisotropy and physical properties in the SAFOD Pilot Hole in Parkfield, CA, *Geophys. Res. Lett.,* **31,** L15S17.

Boness, N.L. & Zoback, M.D., 2006. A mutiscale study of the mechanisms controlling shear velocity anisotropy in the San Andreas fault observatory at depth, *Geophysics,* **71**(5), F131–F146.

Bonilla, M.G., 1977. Summary of quaternary faulting and elevation changes in Taiwan, *Mem. Geol. Soc. China,* **2,** 43–55.

Chang, S.L., 1971. Subsurface geologic study of the Taichung basin, *Petro. Geol. Taiwan,* **8,** 21–45.

Chen, T.N., Zhu, W., Wong, T. & Song, S., 2005. Hydromechanical behavior of country rock samples from the Taiwan Chelungpu-Fault Drilling Project, *Eos Trans. AGU*, **86**(52), Fall Meet. Suppl., Abstract T51A-1324.

Chiang, C.W., Unsworth, M.J, Chen, C.S., Chen, C.C. & Lin, T.S., 2008. Fault zone resistivity structure and monitoring at the Taiwan Chelungpu Drilling Project (TCDP), *Terr. Atmos. Ocean. Sci.*, in press.

Christensen, N.I. & Mooney, W.D., 1995. Seismic velocity structure and composition of the continental crust: A global view, *J. geophys. Res.,* **100,** 9761–9788.

CPC. 1982. *Geologic Map of Western Taiwan, Taichung sheet (1: 100,000)*, TPED, Chinese Petroleum Corporation, Miaoli, Taiwan.

Cornet, F., 2007. The Corinth Rift Laboratory or an in situ Investigation on Interactions between Fluids and Active Faults. *Scientific Drilling*, special issue, **1,** 35–38, doi:10.2204/iodp.sd.s01.20.

Crampin, S., 1986. Anisotropy and transverse isotropy, *Geophys. Prospect.,* **34,** 94–99.

Crampin, S. & Peacock, S., 2005. A review of shear-wave splitting in the compliant crack-critical anisotropic Earth, *Wave Motion,* **41,** 59–77.

Davis, D., Suppe, J. & Dahlen, F.A., 1983. Mechanics of fold-and-thrust belts and accretionary wedges, *J. geophys. Res.,* **88,** 1153–1172.

Dong, J.J, Hsu, J.Y., Wu, Y.H., Hung, J.H. & Yeh, E.C., 2005. The stress-dependent permeability/porosity of drilled cores from TCDP Hole-A, *Eos Trans. AGU*, **86**(52), Fall Meet. Suppl., Abstract T51A-1323.

Dong J.J., Hsu, J.Y., Shimamoto, T., Hung, J.H., Yeh, E.C. & Wu, Y.H., 2008. Elucidating the relation between confining pressure and fluid flow properties of sandstone and shale retrieved from TCDP Hole-A, *Am. Assoc. Petrol. Geolog.,* submitted.

Doveton, J.H., 1994. *Geologic Log Analysis Using Computer Methods*, The American Applications in Geology.

Esmersoy, C., Kane, M., Boyd, A. & Denoo, S., 1995. Fracture and stress evaluation using dipole-shear anisotropy logs, *SPWL Symp. Trans.,* **36,** 12.

Hirono, T. *et al.*, 2007a. Nondestructive continuous physical property measurements of core samples recovered from hole B, Taiwan Chelungpu-Fault Drilling Project, *J. geophys. Res.*, **112,** B07404.

Hirono, T. *et al.*, 2007b. Chemical and isotopic characteristics of interstitial fluids within the Taiwan Chelungpu fault, *Geochm. J.*, **41,** 97–102.

Ho, C.S., 1988. *An Introduction to the Geology of Taiwan—Explanatory Text of the Geologic Map of Taiwan*. Minist. Econ. Aff., Cent. Geol. Surv., Taipei, Taiwan, R.O.C.

Hung, J.H., Zhan, H.P., Wiltschko, D.V. & Fang, P., 2002. Geodetically observation surface displacements of the 1999 Chi-chi earthquake near southern termination of the Chelungpu Fault, *Terr. Atmos. Ocean. Sci.,* **13**(3), 355–366.

Hung, J.H., Wu, Y.H. & Yeh, E.C., 2007. Physical Property, Subsurface Structure and Fault Zone Characteristics in Scientific Drill Holes of Taiwan Chelungpu Fault Drilling Project*, Terr. Atmos. Ocean. Sci.,* **18**(2), 271–293.

Ito, H. & Kiguchi, T., 2005. Distribution and properties of fractures in and around the Nojima Fault in the Hirabayashi GSJ borehole, *Geol. Soc. Lond.,* **240,** 61–74.

Johnson, L.R., 1967. Array measurements of P velocities in the upper mantle, *J. geophys. Res.*, **72,** 6301–6325.

Kano, Y., Mori, J., Fujio, R., Ito, H., Yanagidani, T., Nakao, S. & Ma, K.F., 2006. Heat signature on the Chelungpu fault associated with the 1999 Chi-Chi, Taiwan earthquake, *Geophy. Res. Lett.,* **33,** L14306.

Kao, H. & Chen, W.P., 2000. The Chi-Chi earthquake sequence: active out-of-sequence thrust faulting in Taiwan, *Science,* **288,** 2346–2349.

Kitamura, K., Takahashi, M., Masuda, K., Ito, H., Song, S. & Wang, C., 2005. The relationship between pore-pressure and the elastic-wave velocities of TCDP-cores, *Eos Trans. AGU*, **86**(52), Fall Meet. Suppl., Abstract T51A-1326.

Kuo, L.W. & Song, S.R., 2005. Characteristics of clay minerals in the fault zone of TCDP and its implications, *Eos Trans. AGU*, **86**(52), Fall Meet. Suppl., Abstract T43D-05.

Lallemand, S., Font, Y., Bijwaard, H. & Kao, H., 2001. New insights on 3-D plates interaction near Taiwan from tomography and tectonic implications, *Tectonophysics,* **335,** 229–253.

Lee, J.C. *et al.*, 2001. A vertical exposure of the 1999 surface rupture of the Chelungpu fault at Wufeng, western Taiwan: structural and paleoseismic implications for an active thrust fault, *Bull. seism. Soc. Am.,* **91,** 914–929.

Lee, J. C., Chu, H.T., Angelier, J., Chan, Y.C., Hu, J.C., Lu, C.Y. & Rau, R.J. 2002. Geometry and structure of northern surface ruptures of the 1999 $M_w = 7.6$ Chi-Chi Taiwan earthquake: influence from inherited fold belt structures, *J. Struct. Geol.,* **24,** 173–192.

Lin, W., Yeh, E., Ito, H., Hirono, T., Tanikawa, W., Soh, W., Kinoshita, M. & Hung, J., 2006. Orientation determination of in-situ horizontal principal stresses by using drilling-induced breakouts and tensile fractures in an active fault drilling hole, *Eos Trans. AGU*, **87**(52), Fall Meet. Suppl., Abstract T21D-0449.

Lin, A.T., Wang, S.M., Hung, J.H., Wu, M.S. & Liu, C.S., 2007. Stratigraphy and geology of the Taiwan Chelungpu-fault Drilling Project-A borehole and its neighboring region, central Taiwan, *Terr. Atmos. Ocean. Sci.,* **18**(2), 223–241.

Lin, W. *et al.*, 2007. Current stress state and principal stress rotations in the vicinity of the Chelungpu fault induced by the 1999 Chi-Chi, Taiwan, earthquake, *Geophys. Res. Lett.,* **34,** L16307.

Lockner, D.A., Morrow, C., Song, S., Tembe, S. & Wong, T., 2005. Permeability of whole core samples of Chelungpu fault, Taiwan TCDP scientific drillhole, *Eos Trans. AGU*, **86**(52), Fall Meet. Suppl., Abstract T43D-04.

Lofts, J.C. & Bristow, J.F., 1998. Aspects of core-log integration: an approach using high resolution image, in *Geologic Society, London, Spec. Pub.*, Vol. 136, pp. 273–283, eds Harvey, P. K. & Lovell, M. A., The Geological Society, London.

Louis, L., David, C. & Wong, T.F., 2005. Anisotropy of magnetic susceptibility and P-wave velocity in core samples from the Taiwan Chelungpu-Fault Drilling Project (TCDP), *Eos Trans. AGU*, **86**(52), Fall Meet. Suppl., Abstract T51A-1319.

Lu, C.Y. & Chen, C.W., 2005. Mechanical characteristics of rocks cored from hanging wall of Chelungpu Fault, *Eos Trans. AGU*, **86**(52), Fall Meet. Suppl., Abstract T51A-1318.

Ma, K.F., Song, T.R. A., Lee, S.J. & Wu, H.I., 2000. Spatial slip distribution of the September 20, 1999, Chi-Chi, Taiwan, Earthquake (M_w 7.6)—inverted from teleseismic data, *Geophys. Res. Lett.,* **27**(20), 3417–3420.

Ma, K.F. *et al.*, 2006. Slip zone and energetics of a large earthquake from the Taiwan Chelungpu-fault Drilling Project, *Nature,* **444,** 473–476.

Major, C.O., Pirmez, C. & Goldberg, D., 1998. High resolution core-log integration techniques: examples from the Ocean Drilling Program, in *Geol. Soc., London, Spec. Pub.*, Vol. 136, pp. 285–295, eds Harvey, P. K. & Lovell, M. A., The Geological Society, London.

Malavieille, J., Lallemand, S.E., Dominguez, S., Deschamps, A., Lu, C.Y., Liu, C.S. & Schnürle, P. 2002. Arc-continent collision in Taiwan: New marine observations and tectonic evolution, *Geol. Soc. Am., Spec. Pub.,* **358,** 187–211.

MOEACGS. 2000. *Report of Geological Investigation of 921 Chi-Chi earthquake*, Minist. Econ. Aff., Cent. Geol. Surv., Taipei, Taiwan, R.O.C.

Pathier, E., Fruneau, B., Deffontaines, B., Angelier, J., Chang, C.P., Yu, S.B. & Lee, C.T., 2003. Coseismic displacements of the footwall of the Chelungpu fault caused by the 1999, Taiwan, Chi-Chi earthquake from In SAR and GPS dat, *Earth planet. Sci. Lett.,* **212,** 73–88.

Plumb, R. & Hickman, S., 1985. Stress-induced borehole elongation: a comparison between the four-arm dipmeter and the borehole televiewer in the Auburn geothermal well, *J. geophys. Res.,* **90**(B7), 5513–5521.

Reches, Z. & Ito, H., 2007. Scientific drilling of active faults: Past and future, in *Continental Scientific Drilling: A Decade of Progress and Challenges for the Future*, eds Harms, U., Koeberl, C. and Zoback, M.D. Heidelberg, Germany, Springer, doi:10.1007/978-3-540-68778-8_6.

Schlumberger, 1989. *Log Interpretation Principles/Applications*, Schlumberger Educational Services, Houston, TX.

Schlumberger. 1995. DSI* Dipole Shear Sonic Image: Oilfield Marketing Services. *Schlumberger*, Houston, TX.

Sone, H., Shimamoto, T., Noda, H., Song, S.R., Ma, K.F., Hung, J.H. & Wang, C.Y., 2005. Frictional properties and permeability of fault rocks from Taiwan Chelungpu-fault Drilling Project and their implications for high-velocity slip weakening, *Eos Trans. AGU*, **86**(52), Fall Meet. Suppl., Abstract T43D-06.

Sone, H., Yeh, E.C., Nakaya, T., Hung, J.H., Ma, K.F., Wang, C.Y., Song, S.R. & Shimamoto, T., 2007. Mesoscopic structural observations of cores from the Chelungpu fault system, Taiwan Chelungpu-fault drilling project Hole-A, Taiwan, *Terr. Atmos. Ocean. Sci.,* **18**(2), 359–377.

Song, S.R. & Kuo, L.W., 2006. Slip zone and temperature of faulting in the 1999 Chi-Chi Taiwan earthquake, *Eos Trans. AGU*, **87**(36), West. Pac. Geophys. Meet. Suppl., Abstract S31D-02.

Suppe, J., 1981. Mechanics of mountain building and metamorphism in Taiwan, *Mem. Geol. Soc. China,* **4,** 67–89.

Teng, L.S., 1990. Geotectonic evolution of late Cenozoic arc-continent collision in Taiwan, *Tectonophysics,* **183,** 57–76.

Tezuka, K. & Niitsuma, H., 2000. Stress estimated using microseismic clusters and its relationship to the fracture system of the Hijiori hot dry rock reservoir, *Eng. Geol.,* **56,** 47–62.

Thomsen, L., 1986. Weak elastic anisotropy, *Geophysics*, **51,** 1954–1966.

Wang, C.Y., Chang, C.H. & Ye, H.Y., 2000. An interpretation of the 1999 Chi-Chi earthquake in Taiwan based on the thin-skinned thrust model, *Terr. Atmos. Ocean. Sci.,* **11,** 609–630.

Wang, C.Y., Li, C.L. & Yen, H.Y., 2002. Mapping the northern portion of the Chelungpu fault, Taiwan by shallow reflection seismics, *Geophys. Res. Lett.,* **29**(16), 951–954.

Wang, P.L., Wu, J., Lin, L., Yeh, E.C., Chen, Y. & Song, S., 2005. Isotopic evidence of fluid processes in fault-related rocks from TCDP drill cores in Taiwan, *Eos Trans. AGU*, **86**(52), Fall Meet. Suppl., Abstract T51A-1313.

Wu, H.Y., Ma, K.F., Ito, H. & Hung, J.H., 2005. Stress magnitudes and orientations from geophysical logs and leak-off tests in the Taiwan Chelungpu-Fault Drilling Project, *Eos Trans. AGU*, **86**(52), Fall Meet. Suppl., Abstract T51A-1317.

Wu, J.C., Huang, S., Wang, M., Tsai, C., Mei, W., Hung, J., Lee, T. & Yang, K., 2007. Microfossil analysis of wells in the Chelungpu Fault zone Taiwan, *Terr. Atmos. Ocean. Sci.,* **18**(2), 295–325.

Yabe, Y., Song, S. & Wang, C., 2005. Stress state around Chelungpu Fault, Taiwan, estimated from boring core samples, *Eos Trans. AGU*, **86**(52), Fall Meet. Suppl., Abstract T51A-1316.

Yang, M., Rau, R.J., Yu, J.Y. & Yu, T.T., 2000. Geodetically observed surface displacements of the 1999 Chi-Chi, Taiwan, earthquake, *Earth Planets Space,* **52,** 403–413.

Yeh, E.C. *et al.*, 2007. Preliminary Results of Core Description from the Hole-A of the Taiwan Chelungpu-Fault Drilling Project, *Terr. Atmos. Ocean. Sci.,* **18**(2), 327–357.

Yu, S.B., Chen, H.Y. & Kuo, L.C. 1997. Velocity field of GPS stations in the Taiwan area. *Tectonophysics* **274,** 41–59.

Yu, S.B. *et al*., 2001. Preseismic deformation and coseismic displacement associated with the 1999 Chi-Chi, Taiwan, earthquake, *Bull. seism. Soc. Am.,* **91,** 995–1012.

Yue, L.F., Suppe, J. & Hung, J.H., 2005. Structural geology of a classic thrust belt earthquake: the 1999 Chi-Chi earthquake Taiwan (M_w7.6), *J. Struct. Geol.,* **27,** 2058–2083.

APPENDIX A

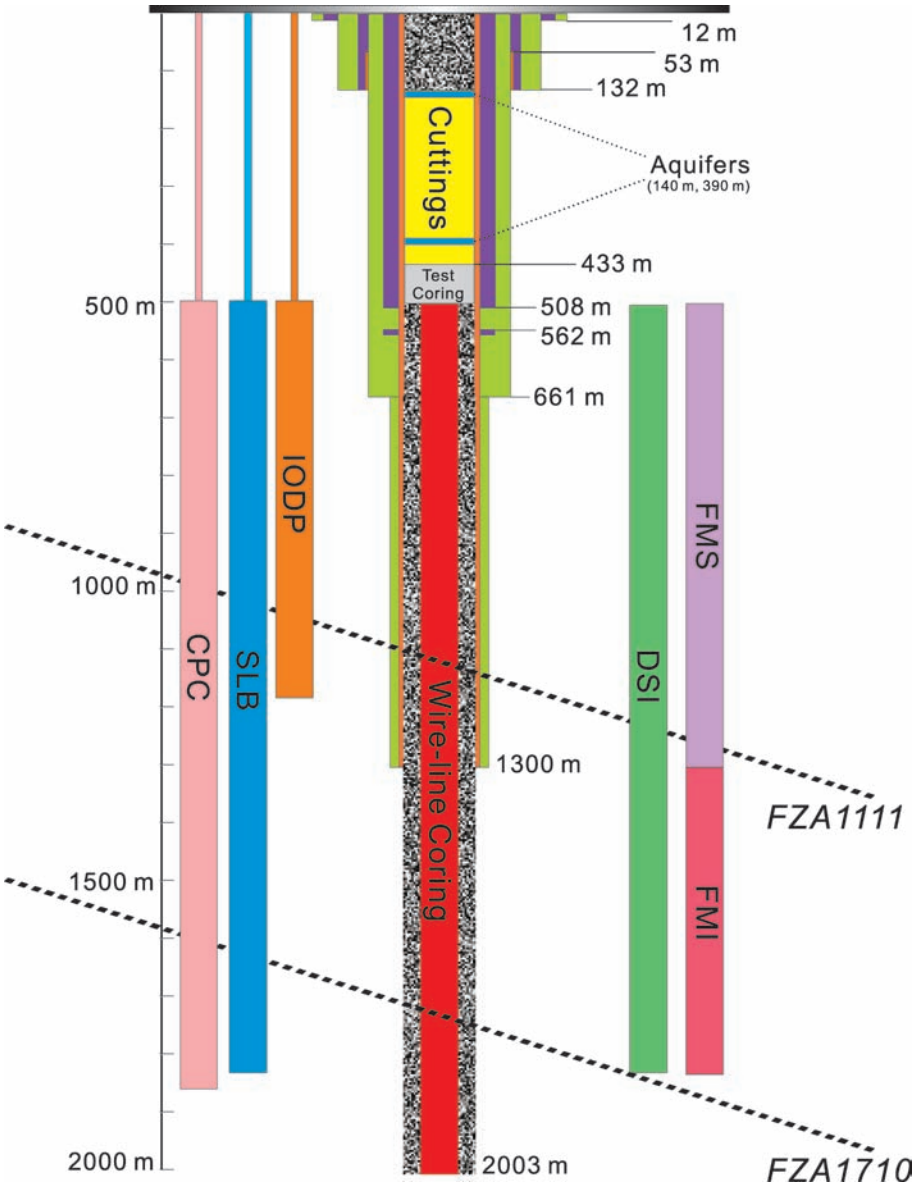

Figure A1. Case plan of Hole-A, 0–12 m 22 inches reaming, 20 inches × 9.52 mm casing; 12–132 m 17.5 inches reaming; 0–132 m 14 inches × 9.52 mm casing; 53–132 m 12.75 inches × 9.52 mm casing; 140–150 m aquifer; 132–661 m 12.25 inches reaming; 390 m aquifer; 0–661 m 9.625 inches × 10 mm casing; 661–1300 m 8.5 inches reaming; 0–1300 m 7 inches × 10 mm casing; 132–433 m cutting; 433–660 m 6 inches coring; one steel case-shoe dropped at 562 m; geophysical logs conducted in hole-A; two major fault zones penetrated in hole-A.

APPENDIX B

Table B1. Types of wire-line logs conducted by three organizations. The intervals shown here are not calibrated to each other. All starting depths are corrected to drilling rotary table, and consequently some of them are higher than ground (depth is negative). In this research, we only use data conducted from CPC and SLB, and all of the logs referenced to the log-depth of SLB. Each of logs is interactively calibrated by using GR (gamma ray log) and integrated with unrolled core-images.

Group	Log Sonde	From (m)	To (m)	Group	Log Sonde	From (m)	To (m)
CPC	CAL-GR	149.55	257.85	SLB	AIT-GR	422.68	1298.30
	(SL, TTRM, DAC)-GR	157.8	260.55		AIT-GR_Repeat section	490.35	635.20
	DAC-GR	157.65	430.05		DSI-GR	499.45	1306.37
	(SL, TTRM, DAC)-GR	243.3	430.05		FMS-GR	497.89	1300.58
	DAC	157.65	432.6		FMS-GR_Repeat section	909.83	1300.12
	(DPIL, TTRM)-GR	175.05	432.9		FMI-GR	1247.00	1304.00
	SL-GR	175.05	432.9		FMI-GR	1218.93	1867.05
	SL	175.05	435.45		FMI-GR_Repeat section	1397.39	1608.43
	(DPIL, TTRM)-GR	−4.95	511.2		TLD_MCFL_CNL	1292.86	1755.95
	(DPIL, TTRM)-GR	−4.65	514.35		TLD_MCFL_CNL_Repeat section	1293.47	1405.13
	(CAL, SL, DPIL, TTRM, DAC)-GR	396.15	1294.65		DSI-GR	1270.10	1883.97
	CAL	1216.8	1845.6	ICDP	(TS-BSDLL)-GR	606	671
	(SL, DPIL, TTRM, DAC)-GR	1241.7	1863.9		FAC40	790	1145
					MP	10	1164
					SGR-GR	497	1164
					(TS-DLL)-GR	496	1177

APPENDIX C

Table C1. The descriptions of the logs plotted in Fig. 3.

Column	Name	Right	Left	Unit	Remark
A	Bit Size	6	6	inches	FMI/FMS
	Caliper1	−3	12	inches	FMI/FMS
	Caliper2	12	−3	inches	FMI/FMS
	Pad 1 Azimuth	0	360	deg	FMI/FMS
β	Deep Resistivity	2	200	Ohm m	CPC-Log scale
	Mid resistivity	2	200	Ohm m	CPC-Log scale
C	Water Saturation	0	1	per cent	–
	Spontaneous Potential	50	75	mV	CPC
	Bulk Volume of Water	0	0.5	–	–
D	Percentage of V_s anisotropy	50	0	–	DSI
	Borehole Temperature	30	60	°C	CPC
E	Gamma ray	0	150	API	CPC
	Interpretated Lithology	–	–	–	–
F	Poisson's Ratio	0	0.5	–	DSI
	V_p/V_s	0	5	–	DSI
G	Delay Time, V_{p-s}	150	50	μs Feet^{-1}	DSI
	Delay Time, V_{s-s}	150	50	μs Feet^{-1}	DSI
	Delay Time, V_{p-c}	150	50	μs Feet^{-1}	CPC
	Density, Rho	3	1	g cm^{-3}	TLD
H	Porosity, Phi-d	0	0.5	per cent	Density-derived
	Porosity, Phi-s	0	0.5	per cent	Sonic-derived
	Porosity-e	0	0.5	per cent	Core-experimented
I	Fracture Density, Fract-d	15	0	–	Single count per meter
	Well Trajectory	0	15	deg	FMI/FMS
J	Fast Shear Horizontal Azimuth	0	180	deg	DSI
K	Borehole Image	0	360	deg	FMS-500–1300 m; FMI-1300–1860 m
L	Fracture Stereonet	–	–	–	Normal-projected
	Rose Diagram of FSH	–	–	–	–

APPENDIX D

Table D1. The descriptions of the logs plotted in Fig. 3.

Unit	Section	Depth interval (m) From	To	Structure	Sequence
I	I-1	500	660	*Casing*	Cholan Formation
	I-2	660	870	Shear zone	
	I-3	870	1013	Sequence boundary	
II	II-1	1013	1111	FZA1111	Chinshui Shale
	II-2	1111	1241	FZA1241	
	II-3	1241	1300	*Casing*	
III	III-1	1300	1525	FZA1525	Kueichulin Formation
	III-2	1525	1581	FZA1581	
	III-3	1581	1712	FZA1712	
IV	–	1712	1860	*Log bottom*	Cholan Formation

APPENDIX E

Table E1. Characters of fault zones, and at a 30 inches penetrating depth of induction resistivity of AIT tool, AT 30, equal to medium induction resistivity, RM and similarly as AT 90, penetrating depth 90 inches, to deep induction resistivity, RD. AIT tool only runs at the interval of 500–1300 m of Hole-A, and we use RM and RD to consisting with log plot Fig. 3

Fault zone	Top depth (m)	Bottom depth (m)	Total width (m)	Upper Damage zone width (m)	Fault core width (m)	Lower Damage zone width (m)	Gouge width (m)	Water content	Lowest AT90/RD (ohm-m)	AT30/RM (ohm-m)	Lowest RD versus RM
FZA1111	1106.29	1111.79	5.5	2.85	2.45	0.2	1.12	High	6.9064	6.5953	RD>RM
FZA1153	1149.30	1155.26	5.59	1.64	2.45	1.46	0.76	Low	8.0716	8.4074	RM>RD
FZA1221	1219.03	1221.93	2.9	1.57	1.26	0.07	0.01–0.05	Few	9.0178	9.4135	RM>RD
FZA1241	1238.38	1244.08	5.7	N/A	N/A	N/A	0.05–0.10	No	10.5815	10.1428	RD>RM
FZA1525	1519.91	1527.73	7.82	0	0.37	0	0.37	Low	10.806	10.181	RD>RM
FZA1581	1580.15	1583.67	3.52	0.15	1.52	1.85	0	High	11.178	8.895	RD>RM
FZA1632	1628.48	1632.38	3.9	1.35	1.58	0.1	0	Medium	22.259	22.106	RD>RM
FZA1679	1678.45	1680.02	1.57	0	1.57	0	0	Few	13.419	13.984	RM>RD
FZA1710	1711.30	1716.65	5.35	0	1.05	3.9	1.05	Medium	7.421	6.678	RD>RM
FZA1825	1823.50	1829.15	5.65	0	0.2	0	0.2	Low	7.788	6.822	RD>RM
FZA1856	1853.70	1856.74	3.04	2.39	0.15	0.5	0.15	Few	9.944	8.555	RD>RM

APPENDIX F

Table F1. Depth interval of FSH-Core fracture inherence boundaries shown in Fig. 3

1		2		3	
From (m)	To (m)	From (m)	To (m)	From (m)	To (m)
500	650	650	800	800	950
4		5		7	
From (m)	To (m)	From (m)	To (m)	From (m)	To (m)
950	1078	1078	1190	1190	1300
7		8		9	
From (m)	To (m)	From (m)	To (m)	From (m)	To (m)
1300	1525	1525	1679	1679	1860